Modulation of turbulence in forced convection by temperature-dependent viscosity

Francesco Zonta, Cristian Marchioli and Alfredo Soldati†‡

Centro Interdipartimentale di Fluidodinamica e Idraulica and Dipartimento di Energetica e Macchine,
Università degli Studi di Udine, Via delle Scienze 208, 33100 Udine, Italy

In this work, we run a numerical experiment to study the behaviour of incompressible Newtonian fluids with anisotropic temperature-dependent viscosity in forced convection turbulence. We present a systematic analysis of variable-viscosity effects, isolated from gravity, with relevance for aerospace cooling/heating applications. We performed an extensive campaign based on pseudo-spectral direct numerical simulations of turbulent water channel flow in the Reynolds number parameter space. We considered constant temperature boundary conditions and different temperature gradients between the channel walls. Results indicate that average and turbulent fields undergo significant variations. Compared with isothermal flow with constant viscosity, we observe that turbulence is promoted in the cold side of the channel, characterized by viscosity locally higher than the mean: in the range of the examined Reynolds numbers and in absence of gravity, higher values of viscosity determine an increase of turbulent kinetic energy, whereas a decrease of turbulent kinetic energy is determined at the hot wall. Examining in detail the turbulent kinetic energy budget, we find that turbulence modifications are associated with changes in the rate at which energy is produced and dissipated near the walls: specifically, at the hot wall (respectively cold wall) production decreases (respectively increases) while dissipation increases (respectively decreases).

Key words: turbulence simulation, turbulent convection

1. Introduction

Prediction of turbulent flows characterized by large temperature gradients and high heat transfer rates is of great importance in engineering. Heat exchangers, combustion chambers, nuclear reactors and cooling systems in electronic devices are just some of the well-known examples in which significant temperature variations typically occur within the flow. Applications relevant for the present study can be found in aerospace systems, which operate in micro-gravity conditions and require liquid-based cooling technologies to meet high thermal transfer demand (Zonta, Marchioli & Soldati 2008; Campolo, Andreoli & Soldati 2009; Lee *et al.* 2010). In these systems, thermal and viscous properties of the liquid are critical design parameters that vary with temperature. In micro heat exchangers, for instance, the required pumping

† Email address for correspondence: soldati@uniud.it

‡ Also at Department of Fluid Mechanics, CISM, 33100, Udine, Italy.

power and momentum transfer are influenced by temperature-dependent viscosity (Lee *et al.* 2010). Similarly, in nanofluids viscosity changes with temperature but also with nanoparticle concentration in a complex way (Maiga *et al.* 2005; Lee *et al.* 2010; Yu *et al.* 2010). Assessing the influence of temperature-dependent viscosity variations separate from those induced by nanoparticles can set a benchmark to evaluate different nanofluid performances (Zonta *et al.* 2008).

For most conventional heat transfer liquids, density, specific heat and (to a lesser extent) thermal conductivity are relatively independent of temperature, whereas viscosity is not. Compared with constant-viscosity flows, this temperature-dependent variation alters velocity profiles and changes important flow quantities such as the Nusselt number and friction factor. In spite of such effects, it is common practice to account for viscosity variations by adjusting constant-viscosity solutions through empirical correction factors which obviously have limited physical and theoretical justification (Buyukalaka & Jackson 1998). In early times, Sieder & Tate (1936) studied experimentally the effect of non-uniform viscosity on heat transfer in heating and cooling pipe flow, and adjusted the constant-viscosity solution with a correction factor defined by the ratio of viscosities evaluated at bulk and wall temperatures, proposing the following correlations for Nusselt number and friction factor: $Nu/Nu_{constant} = (\mu_{bulk}/\mu_{wall})^n$ and $f/f_{constant} = (\mu_{bulk}/\mu_{wall})^{-m}$, where n and m depend on the specific flow conditions. Since then, other experimental studies were performed, and further correlations proposed (see Buyukalaka & Jackson 1998, for a brief review). These works, however, focused mainly on the determination of coefficients n and m for different flow configurations (e.g. channels and pipes), rather than on the characterization of the flow behaviour from a physical viewpoint.

Among analytical and numerical studies dealing with temperature-dependent viscosity problems, a large majority was devoted to the analysis of laminar heat convection. Shin *et al.* (1993) developed a finite-volume algorithm to study laminar heat transfer in a rectangular duct. The authors focused on the numerical prediction of friction factor and Nusselt number when constant flux boundary conditions are enforced at the top and bottom walls, and imposed temperature conditions are prescribed at the sidewalls. Results revealed an increase in the Nusselt number with respect to the case of constant viscosity. Pinarbasi, Ozalp & Duman (2005) studied the influence produced by variations in both thermal conductivity and viscosity of a Newtonian fluid for the case of laminar Poiseuille flow in a two-dimensional channel with constant-temperature boundary conditions. Momentum and energy equations, coupled through the linear dependence of viscosity on temperature, were solved using the Chebyshev collocation method. Non-uniform viscosity and thermal conductivity affected the temperature field, while very scarce effects were observed on the velocity field. A more systematic study to analyse the effect of heating/cooling on the growth of instabilities in turbulent channel flow was performed by Sameen & Govindarajan (2007) who used linear stability analysis to single out the effects of viscous stratification, heat diffusion and buoyancy. Relevant to the present study is the finding that a decrease of viscosity as the wall is approached has a large stabilizing effect on the flow, the opposite being true for viscosity increase. Albeit under different flow conditions (laminar/turbulent transition in Sameen & Govindarajan (2007), fully developed turbulence here), our results lead to similar conclusions.

From the previous review, phenomenological and statistical analyses of turbulent forced convection with variable fluid properties appear not yet complete for Earth and micro-gravity conditions. In this work we run numerical experiments based on direct numerical simulation (DNS) to investigate on the behaviour of turbulence when

the fluid viscosity varies significantly with temperature and gravity is negligible. This study provides useful information on the forced-convection heat transfer processes, but it has been used in further investigations (Zonta, Onorato & Soldati 2012; Zonta 2010) also to benchmark the influence of the different temperature-dependent fluid properties on the flow (e.g. in stratified flows). We observe that, for Earth gravity environments, the influence of variable viscosity may be cancelled (by buoyancy effects and/or variations of thermal expansion coefficient, for instance) but only at Reynolds numbers higher than those considered in this study (Zonta *et al.* 2012).

Simulations are based on a pseudo-spectral solver of the momentum and energy equations coupled by the explicit dependence of viscosity on temperature through an exponential law. The numerical methodology, described in detail in § 2, is applied to turbulent channel flow using water as a working fluid. Different values of the shear Reynolds number, Re_τ, are considered while the Prandtl number is kept constant. The range of Re_τ was chosen taking into account that the viscous term exhibits a Re_τ^{-1} scaling in our methodological framework, and variable viscosity effects are expected to vanish at very large Reynolds number. Therefore, we selected four values of Re_τ in the low/intermediate turbulent range to explore in detail and put accurate boundaries to these effects.

The flow field statistics, presented here for the first time, are discussed in § 3 and compared with those obtained for the same flow configuration with constant viscosity. Results for velocity moments up to fourth order, turbulent kinetic energy (TKE) and shear stress are then linked in a phenomenological causal relationship to coherent flow structures: a mechanistic view of the boundary layer coherent structures is given to provide qualitative evidence of the non-trivial observed statistical behaviour. Finally, the interplay between microscopic transfer parameters (viscosity) and macroscopic turbulence characteristics are explained in connection with the underlying energy production and dissipation mechanisms.

We remark that the variable-property algorithm employed in this work is similar to those developed by Bae, Yoo & Choi (2005), Li *et al.* (2008), Sewall & Tafti (2008) and Kang, Iaccarino & Ham (2009). In all of these cases the viscosity, density and thermal conductivity vary with temperature. However, the main purpose of those works was to validate the algorithm against benchmark numerical studies, analytical solutions and experimental measurements rather than to analyse the effect produced by variable fluid properties on the flow. In particular, Sewall & Tafti (2008) focused on differentially heated cavity flow and unsteady Poiseuille–Bénard flow and used air as a working fluid. Kang *et al.* (2009) considered conjugate heat transfer around a cylinder in a channel heated from below where the working fluid is water, yet its dependency upon temperature is implemented using tabulated data. Bae *et al.* (2005) performed DNSs of turbulent CO_2 fluid at supercritical pressure in heated vertical tubes with low-Mach-number approximation and considering buoyancy effects, whereas Li *et al.* (2008) analysed a similar problem (supercritical CO_2 turbulent flow) in a different geometry (channel flow) and with a fully compressible approach (albeit neglecting buoyancy effects).

2. Governing equations and numerical modelling

With reference to the schematics of figure 1, we consider an incompressible and Newtonian turbulent flow of water in a plane channel with differentially heated walls: the *hot* wall is kept at temperature T_H^* while the *cold* wall is kept at temperature T_C^*. The superscript $*$ is used to denote dimensional quantities. The origin of the
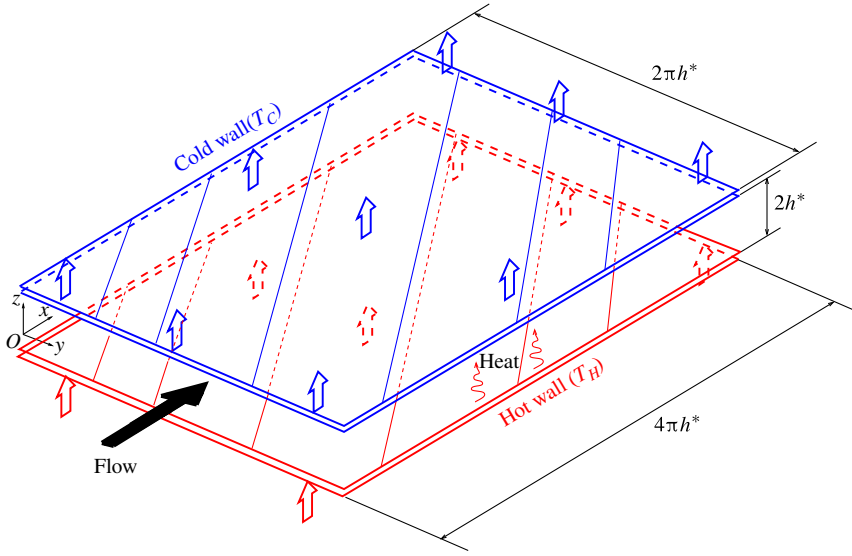
FIGURE 1. (Colour online available at journals.cambridge.org/flm) Sketch of the computational domain.

coordinate system is located at the centre of the channel and x-, y- and z-axes point in the streamwise, spanwise and wall-normal directions, respectively. The size of the channel is $4\pi h^* \times 2\pi h^* \times 2h^*$ in x, y and z, where h^* is the half-channel height. The balance equations are written expressing the fluid viscosity as

$$\mu^*(T^*) = \mu^*_{ref} + \mu^*_v(T^*), \tag{2.1}$$

where μ^*_{ref} is the viscosity at the reference temperature $T^*_{ref} = (T^*_H + T^*_C)/2$, i.e. $\mu^*_{ref} = \mu^*(T^*_{ref}) = 5.494 \times 10^{-4}$ Pa s, and $\mu^*_v(T^*)$ is the local viscosity deviation from μ^*_{ref}. Note that μ^* does not depend explicitly on the shear rate: hence, the fluid can be assumed Newtonian.

All other thermophysical fluid properties (density ρ^*, specific heat c^*_p and thermal conductivity λ^*) are kept constant and are evaluated at T^*_{ref}. This assumption is made primarily because our study focuses on forced-convection heat transfer in zero-gravity conditions and aims at isolating the effect of variable viscosity on the flow field. In the absence of buoyancy and stratification effects, the assumption is further justified within the range of temperature differences between the walls considered in the simulations (and reported in table 1). For the largest temperature difference ($\Delta T^* = T^*_H - T^*_C = 60$ K), the dynamic viscosity varies between $\mu^*|_{293\ K} = 0.98 \times 10^{-3}$ Pa s and $\mu^*|_{353\ K} = 0.347 \times 10^{-3}$ Pa s ($\sim 65\%$ variation), while thermal conductivity varies between $\lambda^*|_{293\ K} = 0.604$ W m^{-1} K^{-1} and $\lambda^*|_{353\ K} = 0.673$ W m^{-1} K^{-1} ($\sim 11\%$ variation). Variation of density and specific heat are even smaller ($\simeq 2.7$ and $\simeq 0.3\%$, respectively).

Based on these arguments, the following set of dimensionless time-dependent variable-viscosity equations is obtained:

$$\frac{\partial u_i}{\partial x_i} = 0, \tag{2.2}$$

	Reynolds number	Grid points	Temperature gradient	Viscosity
		$N_x \times N_y \times N_z$	ΔT (K)	μ^*
S1.1	110	$128 \times 128 \times 129$	—	Constant
S1.2	110	$128 \times 128 \times 129$	40	$\mu = \mu(T)$ — (2.5)
S1.3	110	$128 \times 128 \times 257$	60	$\mu = \mu(T)$ — (2.5)
S2.1	150	$256 \times 256 \times 257$	—	Constant
S2.2	150	$256 \times 256 \times 257$	40	$\mu = \mu(T)$ — (2.5)
S2.3	150	$256 \times 256 \times 257$	60	$\mu = \mu(T)$ — (2.5)
S3.1	180	$256 \times 256 \times 257$	—	Constant
S3.2	180	$256 \times 256 \times 257$	40	$\mu = \mu(T)$ — (2.5)
S3.3	180	$256 \times 256 \times 257$	60	$\mu = \mu(T)$ — (2.5)
S4.1	300	$256 \times 256 \times 257$	—	Constant
S4.2	300	$256 \times 256 \times 513$	60	$\mu = \mu(T)$ — (2.5)

TABLE 1. Summary of the simulation parameters.

$$\frac{\partial u_i}{\partial t} = -u_j \frac{\partial u_i}{\partial x_j} + \delta_{i,1} - \frac{\partial p}{\partial x_i} + \frac{1}{Re_\tau} \left[\left(\frac{\partial^2 u_i}{\partial x_j^2} \right) + \frac{\partial}{\partial x_j} \left(\mu_v \frac{\partial u_i}{\partial x_j} \right) \right], \qquad (2.3)$$

$$\frac{\partial T}{\partial t} = -u_j \frac{\partial T}{\partial x_j} + \frac{1}{Re_\tau Pr} \left(\frac{\partial^2 T}{\partial x_j^2} \right), \qquad (2.4)$$

where u_i is the ith component of the velocity vector, $\delta_{1,i}$ is the mean pressure gradient, p is the fluctuating kinematic pressure, T is temperature, Re_τ is the shear Reynolds number and Pr is the Prandtl number. Note that $\mu_v = \mu_v^*/\mu_{ref}^*$. In our approach, both Re_τ and Pr are macroscopic input parameters defined considering the thermophysical fluid properties at the reference temperature: $Re_\tau = \rho_{ref}^* u_\tau^* h^*/\mu_{ref}^*$ and $Pr = \mu_{ref}^* c_{p,ref}^*/\lambda_{ref}^*$, where u_τ^* is the shear velocity. For isothermal flows with symmetric axial velocity profile, the shear velocity is defined as $u_\tau^* = \sqrt{\tau_w^*/\rho_{ref}^*}$, where τ_w^* is the shear stress at the wall. The problem under investigation, however, is characterized by a non-symmetric distribution of the axial velocity (see §3 for a detailed discussion), and the value of the shear stress is not the same at the two walls. Therefore, the choice of u_τ^* is not trivial. In this study, we exploit the condition of imposed mean pressure gradient $\delta_{1,i}^*$ to compute the shear velocity as $u_\tau^* = \sqrt{\delta_{1,i}^* h^*/\rho_{ref}^*}$. This is equivalent to replacing τ_w^* with $\delta_{1,i}^* h^*$, which is readily obtained by a simple force balance on the entire channel yielding $\delta_{1,i}^* 2h^* = \tau_{w,C}^* + \tau_{w,H}^* = 2\tau_w^*$, where $\tau_{w,C}^*$ (respectively $\tau_{w,H}^*$) is the mean wall shear stress at the cold wall (respectively hot wall), and τ_w^* is the average value between $\tau_{w,C}^*$ and $\tau_{w,H}^*$.

Equations (2.2)–(2.4) are discretized using a pseudo-spectral method based on transforming the field variables into wavenumber space, through Fourier representations for the periodic (homogeneous) directions x and y, and Chebyshev representation for the wall-normal (non-homogeneous) direction z. Note that periodicity in x and y is assumed for both velocity and temperature, while no-slip and constant temperature conditions (Verzicco & Sreenivasan 2008) are imposed at the walls. As commonly done in pseudo-spectral methods, the convective nonlinear terms are first computed in the physical space and then transformed in the wavenumber space using a de-aliasing procedure based on the 2/3 rule; derivatives are evaluated directly in the wavenumber space to maintain spectral accuracy. Once the velocity field
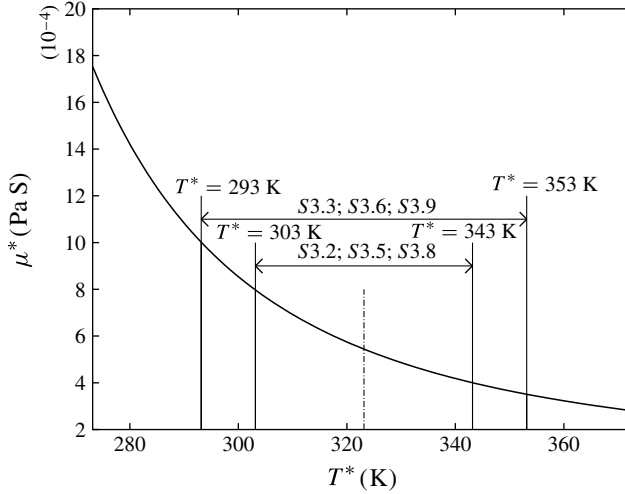
FIGURE 2. Viscosity of water as a function of temperature for $273 < T^* < 373$ K. The temperature differences between the hot wall and the cold wall considered in simulations (*S1.2, S2.2, S3.2*) and (*S1.3, S2.3, S3.3, S4.2*) are also shown.

is known, the temperature field is computed as a solution of the energy equation, and finally viscosity is updated. The procedure is described in detail in Appendix.

Exponential (or Arrhenius-type) relations are usually employed to represent the dependency of viscosity on temperature in analytical and theoretical studies (Sameen & Govindarajan 2007), given the ease of integration. In the present study the following relation was adopted (Popiel & Wojtkowiak 1998):

$$\mu^*(T^*) = A \cdot 10^{B/(T^*-C)} \tag{2.5}$$

because it best matches experimental data (Weast 1988) within the range of temperatures examined. Constants A, B and C are associated with the specific fluid considered. For water, $A = 2.414 \times 10^{-5}$ Pa s, $B = 247.8$ K and $C = 140$ K. A graphical representation of (2.5) is given in figure 2, which shows that the ratio of viscosity values at the walls, $\mu^*(T_C^*)/\mu^*(T_H^*)$, is $\simeq 2$ if $\Delta T^* = 40$ K and $\simeq 2.85$ if $\Delta T^* = 60$ K. Note that (2.5) generates an asymmetric viscosity profile associated with larger viscosity variations at lower temperatures and vice versa.

A summary of the relevant simulation parameters and grid resolutions is given in table 1. Four different values of the reference shear Reynolds number were simulated: $Re_\tau = 110, 150, 180$ and 300. For each value of Re_τ, we performed an extensive code validation against DNS datasets available for the case of uniform and constant fluid viscosity, simply referred to as constant-viscosity simulations hereinafter (Kim, Moin & Moser 1987; Iwamoto, Suzuki & Kasagi 2002; Marchioli *et al.* 2008). All simulations are performed at $Pr = 3$. The spatial resolution is chosen to fulfil the requirements imposed by the DNS. When $Pr > 1$, this choice is driven by the smallest spatial scale of the temperature field, η_θ, which is smaller than the Kolmogorov scale, η_k, in accordance with the following relation (Monin & Yaglom 1975):

$$\eta_\theta \sim \eta_k \left(\frac{1}{Pr}\right)^{1/2}. \tag{2.6}$$

In our simulations we computed $\eta_\theta = 0.577\eta_k$. The streamwise and spanwise grid spacings are $8\eta_\theta < \Delta x < 12\eta_\theta$ and $4\eta_\theta < \Delta y < 6\eta_\theta$ depending on the value of Re_τ, while the wall-normal grid spacing varies from a minimum value $\Delta z_{min} \simeq 10^{-2}\eta_\theta$ at the wall to a maximum value $\Delta z_{max} \simeq 2\eta_\theta$ in the centre of the channel for all values of Re_τ. The spatial resolution was chosen also accounting for the decrease of η_k (and of η_θ) at increasing Re_τ.

3. Results and discussion

To the best of the authors' knowledge, DNSs of turbulent channel flow aimed at evaluation of variable viscosity effects isolated from gravity are not available in the literature. In our simulations, viscosity depends on temperature, which is in turn a function of the wall-normal coordinate. Local changes in viscosity may produce large fluctuations that are expected to influence significantly the turbulent flow, especially in the near-wall region. In the following we try to characterize this influence from a statistical viewpoint. All results are presented considering dimensionless variables in wall units (denoted by superscripts +) obtained normalizing by u_τ^*, ρ_{ref}^* and $\nu_{ref}^* = \mu_{ref}^*/\rho_{ref}^*$.

3.1. *Influence of variable viscosity on fluid velocity statistics*

In this section we analyse the statistical moments of the fluid velocity field up to fourth order. We discuss only results relative to the simulations at $Re_\tau = 110$, since the effects of viscosity we wish to emphasize are qualitatively similar in all cases under consideration but trends become more evident at lower Reynolds numbers.

In figure 3(*a*) wall-normal profiles of the mean streamwise velocity $\langle u_x^+ \rangle$ from simulations with temperature-dependent viscosity (*S*1.2, dashed line; and *S*1.3, dash-dotted line) are compared with the profile obtained with constant viscosity (*S*1.1, solid line). Angular brackets $\langle \ \rangle$ denote averaging in time and over the homogeneous directions. The time window selected to average steady-state statistics is $\Delta T^+ = 2200$. In the $Re_\tau = 110$ simulations this corresponds to $\sim$20 eddy turnover times, defined as $T_{eddy} = h^*/u_\tau^*$. Arrows in this figure, as well as in the following figures, point in the direction of increasing temperature difference between the walls. As apparent from figure 3(*a*), the symmetry of the velocity profile is lost due to the occurrence of higher velocity gradients at the hot wall, favoured by the decrease of viscosity with temperature, and lower gradients at the cold wall, where increased viscosity has a damping effect on the rate of change of $\langle u_x^+ \rangle$ with z^+. The wall-normal profile of the TKE, $\langle E_k^+ \rangle = \langle u_i' u_i' \rangle$ with $u_i' = u_i^+ - \langle u_i^+ \rangle$, is also asymmetric with respect to the geometric channel centreline, as shown in figure 3(*b*). Counterintuitively, turbulence intensity is reduced near the hot wall (up to $\simeq$12 % in terms of peak value), but increased near the cold wall (up to $\simeq$5 % in terms of peak value). Note that the location of the peak for $\langle E_k^+ \rangle$ does not change dramatically for the two cases with temperature-dependent viscosity, since it remains within a distance $z^+ \simeq 20 \div 25$ from the wall. However, compared with the case of constant viscosity, the peak location for $\langle E_k^+ \rangle$ shifts slightly towards the hot wall and away from the cold wall: the behaviour of $\langle u_x^+ \rangle$ and $\langle E_k^+ \rangle$ seems to indicate that the effects due to the increase of viscosity near the cold wall propagate over a proportion of the channel much wider than that influenced by the decrease of viscosity near the hot wall. To appreciate further the effect of temperature-dependent viscosity on turbulence intensities, in figure 4 the root mean square (r.m.s.) of the fluid velocity fluctuations, $\langle RMS(u_i') \rangle$, is shown. Again, profiles are not symmetric and deviations from the constant-viscosity
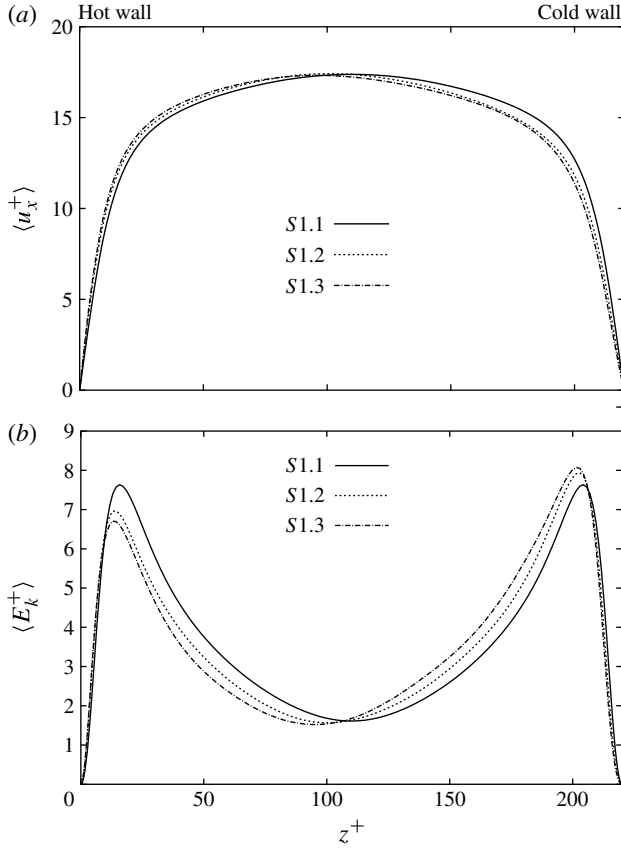
FIGURE 3. (*a*) Mean fluid streamwise velocity $\langle u_x^+ \rangle$ and (*b*) TKE, $\langle E_k^+ \rangle$, at $Re_\tau = 110$: comparison between simulation with constant viscosity (*S*1.1, solid line) and simulations with temperature-dependent viscosity (*S*1.2, dashed line; *S*1.3, dash-dotted line).

situation are evident, particularly in the buffer region. Turbulence intensity decreases in all directions near the hot wall and increases near the cold wall: variations are pronounced in the spanwise direction (figure 4*b*) and in the wall-normal direction (figure 4*c*), where deviations up to 15 % between 'constant' and 'variable' viscosity conditions are observed. This finding is in agreement with previous observations that a reduction in viscosity has a stabilizing effect on boundary layers, whereas an increase in viscosity has a destabilizing effect (Sameen & Govindarajan 2007). This result, obtained from stability analysis, is here demonstrated through the explicit computation of the turbulence intensities.

To emphasize the Re_τ dependency of viscosity variations on turbulence intensities, in figure 5 we compare the behaviour of $\langle RMS(u_i') \rangle$ at increasing Re_τ. Profiles are shown as a function of the normalized wall-normal coordinate z^+/Re_τ. With no stratification effects (as occurs in zero-gravity conditions), variable-viscosity effects become less significant as Re_τ increases in agreement with the Re_τ^{-1} scaling prescribed by (2.3). We quantified this trend computing

$$\Delta_{RMS}[\%] = \frac{\langle RMS(u_i') \rangle_{\mu=var} - \langle RMS(u_i') \rangle_{\mu=const}}{\langle RMS(u_i') \rangle_{\mu=const}}. \tag{3.1}$$
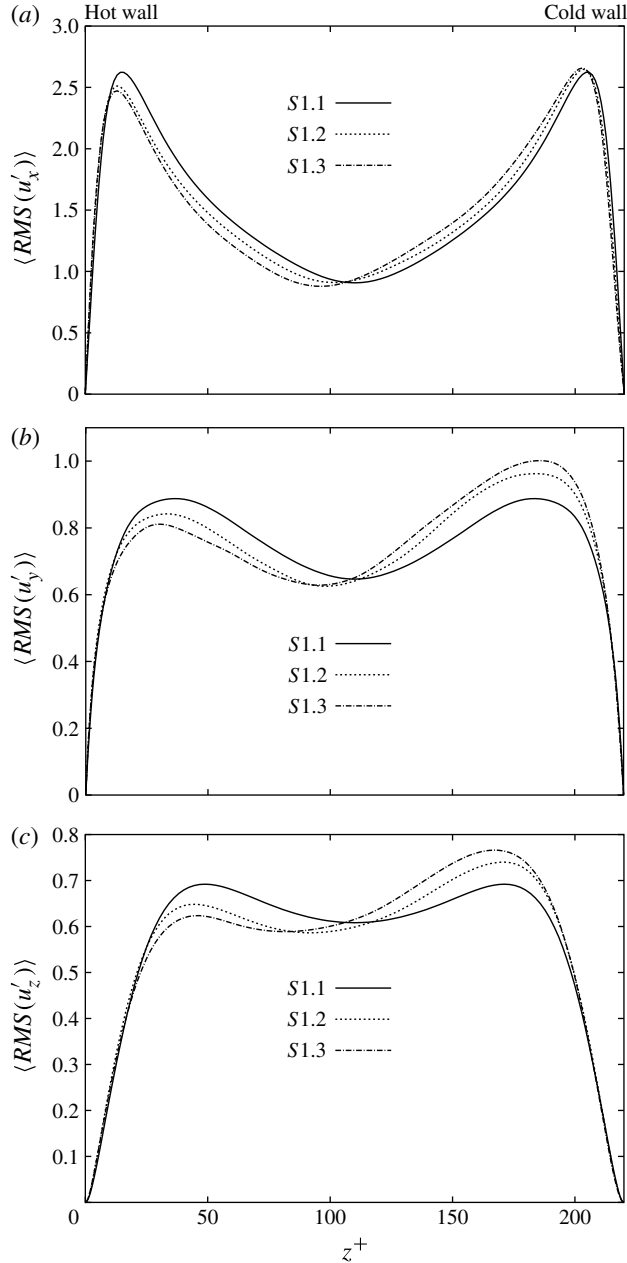
FIGURE 4. Root mean square of fluid velocity fluctuations at $Re_\tau = 110$: (*a*) streamwise component, $\langle RMS(u'_x) \rangle$; (*b*) spanwise component, $\langle RMS(u'_y) \rangle$; (*c*) wall-normal component, $\langle RMS(u'_z) \rangle$. Lines are as in figure 3.

where $\langle RMS(u'_i) \rangle_{\mu=var}$ refers to the *i*th variable-viscosity r.m.s. component and $\langle RMS(u'_i) \rangle_{\mu=const}$ to its constant-viscosity counterpart. The behaviour of $\Delta_{RMS}[\%]$ is shown in figure 5(*d*) for the wall-normal r.m.s. component: the decrease of turbulence intensity modulation due to viscosity at $Re_\tau = 300$ is evident. Similar results are
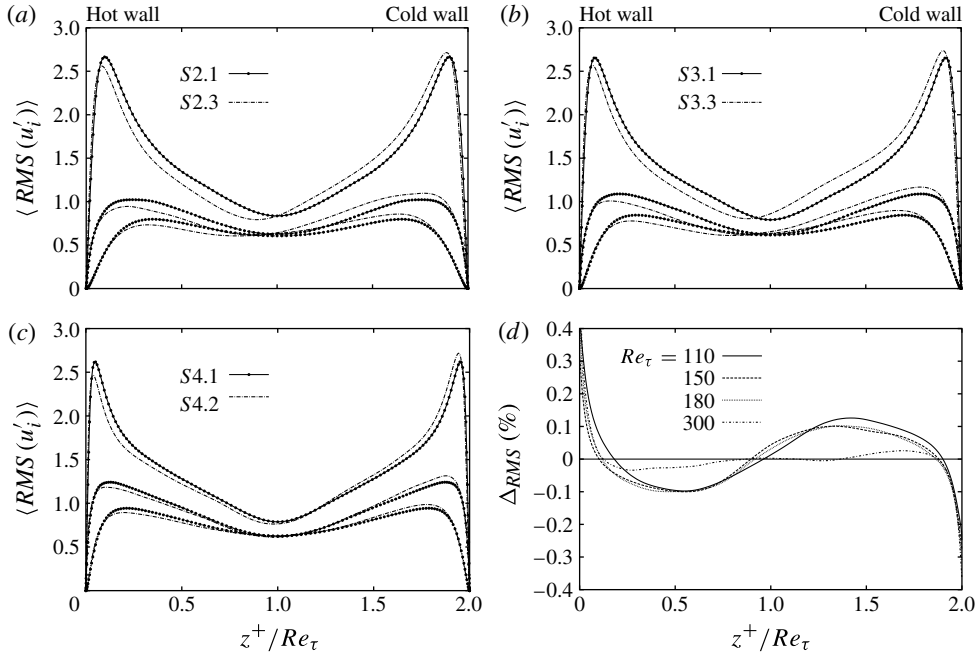
FIGURE 5. Root mean square of fluid velocity fluctuations at varying Reynolds number: (*a*) $Re_\tau = 150$; (*b*) $Re_\tau = 180$; (*c*) $Re_\tau = 300$. Variable-viscosity results (dash-dotted lines) are contrasted with constant-viscosity results (symbols). The relative per cent change of the wall-normal r.m.s. values (taken here as a reference) with Re_τ is quantified by $\Delta_{RMS}[\%]$ in (*d*).

obtained for the other components. We remark that the low-Re_τ effects on turbulence intensities discussed here for zero-gravity conditions have been observed also in stably stratified wall-bounded flow, where Earth gravity conditions apply (Zonta *et al.* 2012).

Finally, the higher-order moments (skewness and flatness) are shown in figure 6. Significant viscosity effects are observed in the streamwise and wall-normal directions. The skewness factor of the fluid velocity fluctuations, $\langle S(u_i')\rangle$, is shown in figure 6(*a,b*). A high positive value of the skewness means that velocity fluctuations more frequently attain large positive rather than negative values, the opposite being true for negative skewness. For the streamwise component (figure 6*a*), the turbulent channel flow in the constant-viscosity simulation exhibits more frequent large positive fluctuations at the wall and more frequent large negative fluctuations in the channel centre. The main effect of variable viscosity is to increase the skewness in the near-wall region: this effect is limited to few wall units at the hot wall, but extends to the entire buffer region at the cold side. Note that the maximum value of $\langle S(u_x')\rangle$ at the cold wall is shifted by roughly 5 wall units away from the wall. The skewness of the wall-normal fluctuations ($\langle S(u_z')\rangle$, figure 6*b*), appears shifted towards the hot side when viscosity is allowed to change with temperature. The increase (in magnitude) of $\langle S(u_z')\rangle$ in the wall proximity may indicate higher dissipation (Soldati & Banerjee 1998). High positive fluctuations are a typical signature of coherent *sweep* events that bring high-speed fluid towards the wall and produce high shear-stress regions at the wall. In the present case, higher skewness may indicate an increase either in the number of sweeps or in their intensity, leading in both cases to shear stress production. The reader is referred to § 3.3.2 for further discussion of these issues.
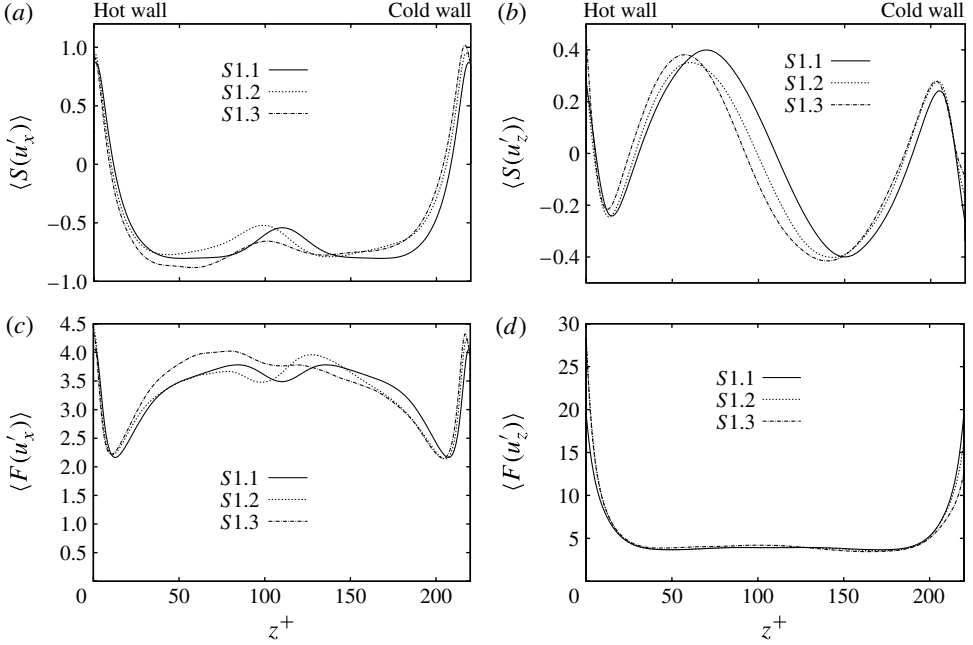
FIGURE 6. Skewness and flatness of fluid velocity fluctuations at $Re_\tau = 110$: (*a*) streamwise component of skewness, $\langle S(u'_x) \rangle$; (*b*) wall-normal component of skewness, $\langle S(u'_z) \rangle$; (*c*) streamwise component of flatness, $\langle F(u'_x) \rangle$; (*d*) wall-normal component of flatness, $\langle F(u'_z) \rangle$. Lines are as in figure 3.

The flatness of the velocity fluctuations, $\langle F(u'_i) \rangle$, is shown in figure 6(*c,d*). A *normal* distribution has a flatness factor equal to 3. Higher values of the flatness factor are observed for the streamwise fluctuations near the cold wall, particularly when the temperature gradient increases. This indicates that fluctuations are often larger than the variance of the distribution and have a more intermittent character. As already observed for $\langle S(u'_x) \rangle$, also the flatness factor attains a maximum at ~ 5 wall units from the cold wall. The flatness of the wall-normal component (figure 6*d*) decreases near the cold wall and increases near the hot wall (up to $\simeq 40\%$ variations for $\langle F(u'_z) \rangle$ in the $S1.3$ simulation), while remaining substantially unchanged in the centre of the channel. A high/low flatness factor value is an indicator of the high/low intermittent character of the velocity fluctuations: in the wall-normal direction, in particular, it gives an indication of the intermittent nature of the Reynolds shear stress producing events near the wall. From a quantitative viewpoint, the intensity of these events can be quantified using the non-dimensional (i.e. normalized by $\rho^*_{ref} u^{*2}_\tau$) turbulent shear stress $\tau^t_{xz} = -\rho \langle u'_x u'_z \rangle$, where $u'_x u'_z$ is the instantaneous fluctuating Reynolds stress in the longitudinal x–z plane. We remind that $\rho = \rho^*/\rho^*_{ref} = 1$ in our simulations. The behaviour of τ^t_{xz} along the wall-normal direction is shown in figure 7(*a*), together with the total shear stress of the fluid $\tau^{tot}_{xz} = \tau^t_{xz} + \tau^v_{xz}$, where

$$\tau^v_{xz} = -\langle \mu \rangle \frac{\partial \langle u^+_x \rangle}{\partial z^+} \frac{1}{Re_\tau}, \tag{3.2}$$

is the viscous shear stress. In (3.2), $\mu = \mu^*/\mu^*_{ref}$ is a function of temperature and $\partial \langle u^+_x \rangle / \partial z^+$ is the mean strain rate. The contribution $\langle \mu'(\partial u'_x / \partial z) \rangle$ to τ^v_{xz} due to the
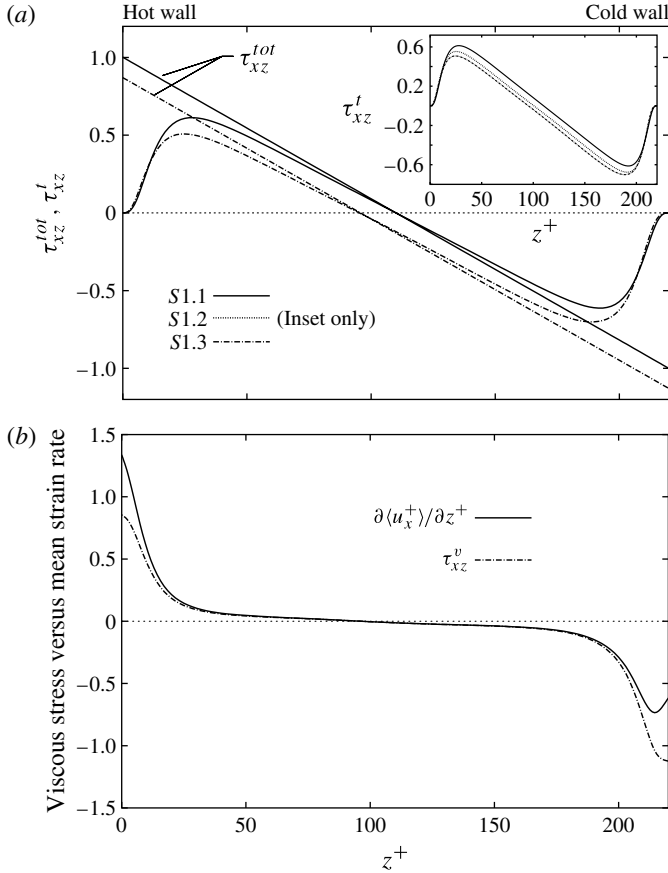
FIGURE 7. (*a*) Wall-normal behaviour of the total shear stress, τ_{xz}^{tot}, and of the turbulent shear stress, τ_{xz}^{t}, with/without temperature-dependent viscosity at $Re_\tau = 110$ (simulations $S1.1$ and $S1.3$). (*b*) Wall-normal behaviour of the viscous shear stress, τ_{xz}^{v}, and of the mean strain rate, $\partial \langle u_x^+ \rangle / \partial z^+$, for simulation $S1.3$.

fluctuating component of viscosity was found to be negligible: hence, it was not included in (3.2) (see also Bae *et al.* 2005). As apparent from figure 7(*a*), the shape of the stress profiles is qualitatively similar for all simulations at $Re_\tau = 110$ (indeed, such similarities are observed for all of the values of Re_τ examined). Viscosity variations shift the profiles towards lower values. The peak value of τ_{xz}^{t} decreases near the hot wall (roughly -15% for simulation $S1.3$), indicating the lower intensity of the stress-producing events; conversely, the peak value increases in magnitude near the cold wall (roughly $+15\%$ for simulation $S1.3$), indicating higher event intensity. No such effect is observed within the viscous sublayer, in agreement with the behaviour of the skewness in the streamwise direction. As already observed for the r.m.s. profiles, the location of the peak of τ_{xz}^{t} is slightly displaced ($\simeq 5$ wall units): towards the channel centreline for the negative peak, and towards the wall for the positive peak.

As far as the total shear stress is concerned, the behaviour in the constant-viscosity case is well known: τ_{xz}^{tot} varies linearly in the range ± 1 vanishing at the geometric channel centreline $z^+ = 110$. With variable viscosity, profile is still linear, but not symmetric with respect to the centreline: we obtain $\tau_{xz}^{tot} < 1$ at the hot wall, $\tau_{xz}^{tot} = 0$ at

$z^+ \simeq 95$ and $|\tau_{xz}^{tot}| > 1$ at the cold wall. Owing to macroscopic force balance, the shear surplus at the cold side is balanced by the shear deficit at the hot side.

The changes just described are consistent with those already observed for the mean streamwise velocity (figure 3a), and are produced by a change of both τ_{xz}^t (dash-dotted line in figure 7(a) and τ_{xz}^v. This latter contribution is shown in figure 7(b) together with the mean strain rate to highlight the interesting behaviour caused by variable viscosity. In the hot side of the channel, both viscous stress and strain rate reach their peak value right at the wall. The viscous stress, however, attains a lower value due to the decrease of viscosity with temperature. In the cold side of the channel, the viscous stress is still maximum at the wall but the strain rate reaches its negative peak away from the wall. This is associated with the occurrence of an inflection point and an inversion of slope in the strain rate profile. Figure 7(b) indicates clearly that, with variable viscosity, the wall-normal shear stress is determined by the local balance between mean shear (which actually decreases very near the cold wall) and viscosity (which strongly increases due to lower fluid temperature). Building on this datum we will show later that a change of viscosity alters significantly the transport mechanisms near the cold wall, leading to an off-the-wall shift of the location at which macroscopic transfer coefficients are maximized.

3.2. *Influence of variable viscosity on the bulk Reynolds number*

Previous observations of the decrease (respectively increase) of turbulence intensity near the hot wall (respectively cold wall) seem counterintuitive. A first-glance reasoning would be the following: in pipe/channel flow, when viscosity is reduced inertial effects are less damped and fluctuations are bound to increase. By analogy, one would expect the same reasoning to hold for the two sides of the channel and would intuitively justify a behaviour of turbulence opposite to that we found. We try to justify our findings with simple scaling arguments to show that in zero-gravity conditions the above intuitive reasoning is indeed wrong. To discriminate variable-viscosity effects on the boundary layer structure, we can subdivide the flow domain into two distinct subchannels, one on the hot side and the other on the cold side, separated by the x–y plane where the mean shear stress vanishes (located at $z^+ = 95$ in the reference simulation $S1.3$). For each subchannel, we obtain the following bulk Reynolds numbers:

$$Re_b^{cold} = \frac{u_b^{cold} 4h^{cold} \rho_{ref}}{\mu_b^{cold}} = 3356, \tag{3.3}$$

$$Re_b^{hot} = \frac{u_b^{hot} 4h^{hot} \rho_{ref}}{\mu_b^{hot}} = 3084. \tag{3.4}$$

In the above equations, $h^{cold} = 2.27 \times 10^{-2}$ m and $h^{hot} = 1.73 \times 10^{-2}$ m are the heights of each subchannel, $u_b^{cold} = 4.34 \times 10^{-2}$ m s^{-1} and $u_b^{hot} = 4.43 \times 10^{-2}$ m s^{-1} are the bulk velocities and $\mu_b^{cold} = 5.818 \times 10^{-4}$ Pa s and $\mu_b^{hot} = 4.925 \times 10^{-4}$ Pa s are the bulk viscosities. All of the above quantities are expressed in dimensional units (superscript $*$ has been suppressed for ease of notation) and space-averaged over the corresponding subchannel height. Based on equation (3.3) and (3.4), we can conclude that, when the pressure gradient that drives the flow is imposed, the mass flow rate in the cold subchannel is higher than the mass flow rate in the hot subchannel. We have examined also the variation of inertial forces, F_I, and viscous forces, F_V, in the two subchannels. With straightforward meaning of symbols the following scaling holds:

$$F_I \sim \rho_{ref} u_b^2 h^2; \quad F_V \sim \mu_b(u_b/h)h^2. \tag{3.5}$$

Upon computation of these forces in each subchannel, at $Re_\tau = 110$ we obtain

$$\frac{F_V^{cold}}{F_V^{hot}} = 1.52; \quad \frac{F_I^{cold}}{F_I^{hot}} = 1.69. \tag{3.6}$$

As expected, in the cold subchannel there is a significant increase of the viscous forces ($+52\%$) due to the increase of viscosity. However, there is an even larger increase of the inertial forces ($+69\%$), in agreement with the values of Re_b^{cold} and Re_b^{hot}. This is mostly due to the cold subchannel extending over a much wider wall-normal proportion of the flow domain. For increasing Re_τ, both force ratios should converge to unity and the flow symmetry should be recovered. In our simulations we obtain $h^{cold}/h^{hot} \simeq 1.31, 1.28, 1.25$ and 1.05 at $Re_\tau = 110$ ($S1.3$), 150 ($S2.3$), 180 ($S3.3$) and 300 ($S4.2$). This result confirms that the variable-viscosity effects we observe will fade out at higher Reynolds numbers.

3.3. *Influence of variable viscosity on instantaneous turbulence structures*

The aim of this section is to provide causal connection between the statistical results of § 3.1 and the dynamics of the turbulence coherent structures. We consider those structures that are important to sustain the regeneration cycle of near-wall turbulence: low-speed streaks, bursting events (i.e. sweeps and ejections) and quasi-streamwise vortices. For details on the turbulence regeneration mechanisms, we refer the reader to Adrian (2007) and Soldati (2005) and references therein. As before, results are shown only for reference simulations at $Re_\tau = 110$ to simplify the discussion.

3.3.1. *Low-speed streaks*

Fluid velocity streaks are shown in figure 8 for the cold wall (figure 8*a*) and for the hot wall (figure 8*b*), respectively. A greyscale mapping is used for the instantaneous streamwise fluid velocity fluctuations u'_x taken in the wall-parallel x–y plane located at a distance $z^+ = 5$ from each wall. Dark-grey areas indicate regions of negative u'_x and mark the location of low-speed streaks, light-grey areas indicate regions of positive u'_x and mark the location of high-speed streaks. Low-speed streaks appear to be stronger, more pronounced (as shown by the steeper greyscale gradients) and arguably more persistent at the hot wall. This is in agreement with the behaviour of the strain rate shown in figure 7: near the hot wall strain is increased slightly yet enough to favour streak formation, with an opposite behaviour near the cold wall. The persistence of the streaks, defined by their extent in the wall-normal direction, is connected directly to the local shear rate and to the turbulent dissipation rate. In § 3.4, we provide a criterion to quantify modification of streak persistence due to variable viscosity.

3.3.2. *Sweeps, ejections and quadrant analysis*

Quantitative information on sweeps and ejections are obtained through quadrant analysis of the $-\langle u'_x u'_z \rangle$ component of the Reynolds stress tensor (Willmarth & Lu 1972). Results are shown in figure 9, where lines and symbols refer to Reynolds stress contributions in the hot subchannel and in the cold subchannel, respectively. Here we are specially interested in quadrants II ($u'_x < 0$, $u'_z > 0$) and IV ($u'_x > 0$, $u'_z < 0$), since quadrants I ($u'_x > 0$, $u'_z > 0$) and III ($u'_x < 0$, $u'_z < 0$) correspond to isolated events with low occurrence frequency. In the near wall region, sweep events predominate over the ejection events. Far from the wall the situation reverses, and there is dominance of ejection. The scenario just described is observed also in the simulations at higher Re_τ and is qualitatively similar to that observed in constant-viscosity flows (Willmarth & Lu 1972). The cross-over point from 'sweep dominance' to 'ejection dominance' occurs at $z^+ \simeq 14$ for the constant-viscosity simulations, this location changing only

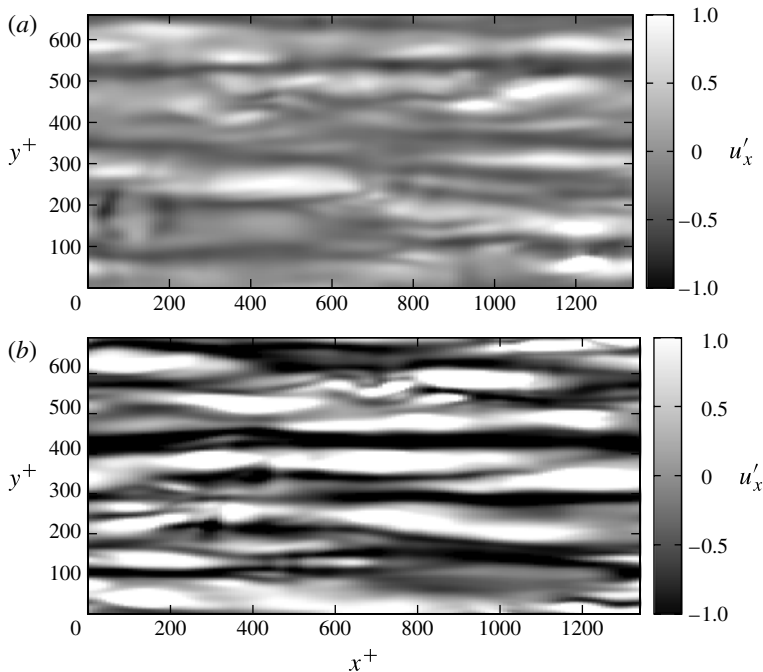FIGURE 8. Velocity streaks in the near-wall region of the channel for flow with temperature-dependent viscosity at $Re_\tau = 110$ (simulation $S1.3$): (*a*) cold wall; (*b*) hot wall. Velocity contours are taken on a wall-parallel plane located at $z^+ = 5$ from the wall.

slightly with the Reynolds number. With temperature-dependent viscosity, the cross-over changes significantly: at $Re_\tau = 110$, the cross-over occurs at $z^+ \simeq 12$ near the hot wall and at $z^+ \simeq 18$ near the cold wall. A larger region of ejection dominance corresponds to lower shear stress generated near the hot wall, the opposite holding near the cold wall, where the stress is generated by stronger (albeit less frequent) sweeps impinging on the wall. This result provides a mechanistic explanation for the shear stress behaviour shown in figure 7.

Strong sweeps/ejections are quasi-periodic events with a characteristic frequency, its inverse corresponding to the time elapsed between subsequent events, indicated here as t^+_{elaps}. In our constant-viscosity simulations we compute $t^+_{elaps} \simeq 80$ at $Re_\tau = 300$ (simulation $S4.1$) and $t^+_{elaps} \simeq 120$ at $Re_\tau = 110$ (simulation $S1.1$), in agreement with the fact that bursting activity is expected to increase with the flow Reynolds number (see Luchik & Tiederman 1987). To benchmark against these values, we also computed t^+_{elaps} in the simulations with temperature-dependent viscosity. Computations were made recording the mean time span between two consecutive sweeps or two consecutive ejections at both walls, over the sampling period $\Delta t^+ \simeq 2200$. Such sampling period was estimated *a priori* to be long enough to cover at least 10 characteristic times t^+_{elaps}, and allowed us to post-process more than 100 instantaneous realizations of the flow field. Following previous works (Lombardi, De Angelis & Banerjee 1996; Marchioli & Soldati 2002), we focused on strongly coherent events occurring in the fluid layer between the wall and the plane at $z^+ \simeq 18$, where the inversion from sweeps-dominance to ejections-dominance is recorded near the cold wall at $Re_\tau = 110$. Results are shown in figure 10 in the form of probability density
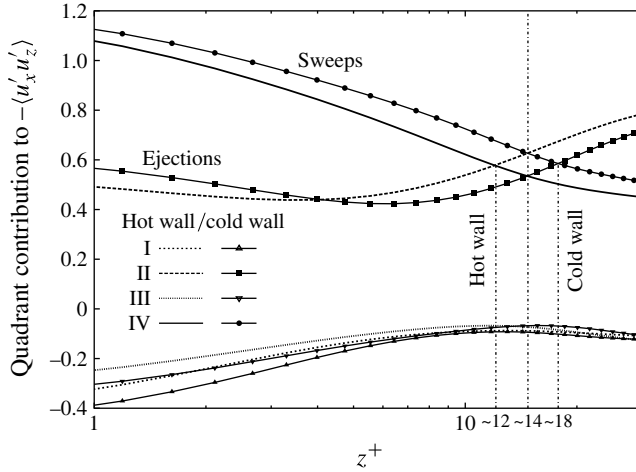
FIGURE 9. Quadrant analysis for channel flow with temperature-dependent viscosity (reference simulation: $S1.3$, $Re_\tau = 110$). Quadrant contributions are identified by Roman numerals: I, II (ejections), III and IV (sweeps).
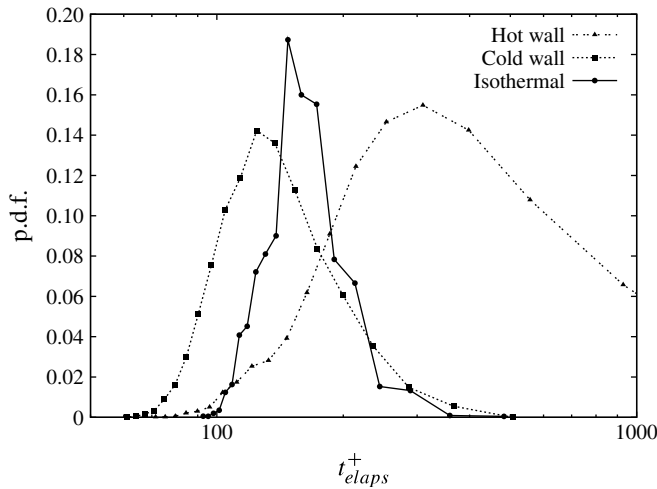

FIGURE 10. Probability density functions of *strongly coherent* sweep/ejection events versus the mean time between consecutive events, t_{elaps}^+. Results refer to simulation $S1.1$ for the constant-viscosity case ($-\bullet-$) and to simulation $S1.3$ for the temperature-dependent viscosity case ($-\blacktriangle-$, hot wall; $-\blacksquare-$, cold wall).

function (p.d.f.). It is observed that bursts become more frequent at the cold wall and less frequent at the hot wall, confirming that turbulence increases locally in regions of higher fluid viscosity. This finding is consistent with the statistical results discussed in the previous sections. Examining further the shape of the different curves, it can be noticed that the variance of t_{elaps}^+ increases and the p.d.f. spreads more around the most probable value when viscosity is allowed to change with temperature. This is particularly evident near the hot wall where tails of the probability distribution become

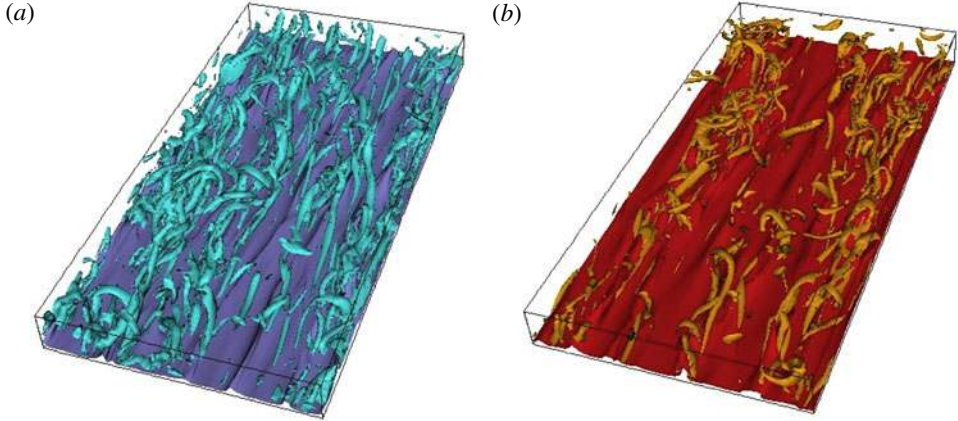(a)   (b)

FIGURE 11. (Colour online) Near-wall vortices in turbulent channel flow with variable viscosity. The reference simulation for visualizations is simulation $S1.3$ ($Re_\tau = 110$). Vortices are rendered as isosurfaces of the absolute value of the streamline rotation vector: $\|\Omega\|/\|\Omega_{max}\| = 0.16$. The values of Ω_{max} in the cold/hot side of the channel were used to normalize $\|\Omega\|$. (a) cold side; (b) hot side. Isosurfaces of the near-wall fluid temperature are also plotted $(((T^* - T_{ref}^*)/\Delta T^*) \pm 0.45)$.

remarkably broad, indicating that the spectrum of bursting frequencies is sampled more homogeneously.

3.3.3. *Near-wall vortical structures*

The vortical structures that can be identified in our channel flow are shown in figure 11, superposed to isosurfaces of the near-wall fluid temperature. Vortices are visualized using the streamline rotation vector $\boldsymbol{\Omega}$ (Perry & Chong 1987), which is particularly suited for regions of the flow with high shear rate (Pan & Banerjee 1995). In vector form:

$$\boldsymbol{\Omega} = -\lambda_i \frac{\boldsymbol{e}_a}{|\boldsymbol{e}_a|} \frac{\boldsymbol{e}_a \cdot (\boldsymbol{r} \times \boldsymbol{c})}{|\boldsymbol{e}_a \cdot (\boldsymbol{r} \times \boldsymbol{c})|}, \tag{3.7}$$

with λ_i the imaginary part of the complex eigenvalues of the velocity gradient tensor, $\boldsymbol{r}$ and $\boldsymbol{c}$ are real and imaginary part of the conjugate complex eigenvectors corresponding to the complex eigenvalues and $\boldsymbol{e}_a$ eigenvector corresponding to the real eigenvalue.

The prominent structures in figure 11 are quasi-streamwise vortices confined within ~ 100 wall units of the boundary. Their streamwise length varies up to ~ 400 shear-based units, in agreement with previous findings for channel flow with constant fluid viscosity (Bernard, Thomas & Handler 1993). Observing figure 11, we notice that vortical structures are larger near the cold wall, which is also more densely populated. In this region turbulence levels are lower and spots of incoherent turbulence are attenuated, confirming that turbulent activity is higher in the cold side of the channel where stronger and more frequent bursting phenomena occur (see figure 10). The behaviour of the thermal structures is essentially the same, due to the analogy existing among transport of momentum and heat.

3.4. *Influence of variable viscosity on TKE balance*

In this section, we examine the TKE balance. We consider the following transport equation of the ensemble-averaged TKE, $\langle k \rangle = \frac{1}{2}\langle u_i' u_i' \rangle$, to analyse the Reynolds stress

transport processes that take place within the flow:

$$\frac{\mathrm{D}\langle k \rangle}{\mathrm{D}t} = \underbrace{-\langle u_i' u_j' \rangle \frac{\partial \langle u_i \rangle}{\partial x_j}}_{P_k} \underbrace{- \frac{1}{\rho} \frac{\partial \langle p' u_i' \rangle}{\partial x_i}}_{\Pi_k} + \underbrace{\frac{1}{\rho} \left\langle p' \frac{\partial u_i'}{\partial x_i} \right\rangle}_{\Phi_k}$$

$$\times \underbrace{- \frac{1}{2} \frac{\partial \langle u_i' u_i' u_j' \rangle}{\partial x_j}}_{T_k} + \underbrace{\frac{1}{2} \frac{\partial}{\partial x_j} \left[\nu(z) \frac{\partial \langle u_i' u_i' \rangle}{\partial x_j} \right]}_{D_k} \underbrace{- \nu(z) \left\langle \frac{\partial u_i'}{\partial x_j} \frac{\partial u_i'}{\partial x_j} \right\rangle}_{\epsilon_k}. \qquad (3.8)$$

Terms on the right-hand side of (3.8) represent the rate of TKE production by mean flow (P_k), pressure diffusion (Π_k), pressure–strain correlation (Φ_k), turbulent diffusion (T_k), viscous diffusion (D_k) and viscous dissipation rate (ϵ_k). Note that the expression used for D_k and ϵ_k in (3.8) refers to the condition of variable fluid viscosity. The material rate of change of $\langle k \rangle$ on the left-hand side of (3.8) is zero since the flow is statistically steady and homogeneous in the streamwise and spanwise directions, with the mean pressure gradient driving the flow being imposed in the streamwise direction (Soldati & Banerjee 1998). Also, $\Phi_k = 0$ from continuity.

Profiles of all non-zero terms included in (3.8) are shown in figure 12. All terms are normalized by $(u_\tau^*)^4 / \nu_{ref}^*$. For validation purposes, in figure 12(a) we compare our constant-viscosity results (symbols) to those previously published by Iwamoto *et al.* (2002) for the same Re_τ (solid lines). In this case, $D_k = 1/2\nu \partial^2 \langle u_i' u_i' \rangle / \partial x_j \partial x_j$ and $\epsilon_k = -\nu \langle \partial u_i' / \partial x_j \, \partial u_i' / \partial x_j \rangle$. Figure 12(a) highlights some known features of TKE redistribution in channel flow when the viscosity of the fluid does not change with temperature. Energy for the velocity field is supplied to the fluid by the action of the mean flow through production P_k. This energy can be either dissipated directly by molecular viscosity (ϵ_k) or converted into turbulent velocity fluctuations (D_k). Energy is received entirely by the streamwise component and is transferred to the other components: mean flow energy derived from the imposed pressure gradient is convected to the wall by turbulence and once in the near-wall region, production increases due to the presence of large mean velocity gradients (i.e. large $\partial \langle u_x^+ \rangle / \partial z^+$). Outside the buffer layer, dissipation is balanced by production in the region $40 < \|z^+ - z_{wall}\| < 100$, and by turbulent transport in the region $100 < z^+ < 120$.

To analyse possible changes in TKE redistribution with variable viscosity, we examine figure 12(b). Particular emphasis is put on production and dissipation, which are the terms most affected by viscosity variations: for ease of comparison, the constant-viscosity profiles of P_k and ϵ_k are plotted again using the same symbols as in figure 12(a). The main conclusion that can be drawn from figure 12(b) is that peak production of TKE decreases near the hot wall and increases near the cold wall. This is in agreement with the finding that turbulence is damped at the hot wall and promoted at the cold wall (see also figure 4). In the hot side of the channel, dissipation decreases outside the viscous sublayer but increases right at the wall where ϵ_k is maximum. This is a direct consequence of the high-velocity fluctuation gradients in this region (ϵ_k is proportional to such gradients by definition). In the cold side of the channel, the behaviour is opposite: dissipation increases outside the viscous sublayer and decreases sharply at the wall. Two local peaks of dissipation (relative maxima) occur at roughly 5 and 15 wall units from the cold wall. Near the cold wall, the dissipation profile develops one additional inflection point, and in turn an additional inversion of slope, not observed near the hot wall. Such behaviour is common to all simulations with variable viscosity and can be ascribed to the sharper rate of change
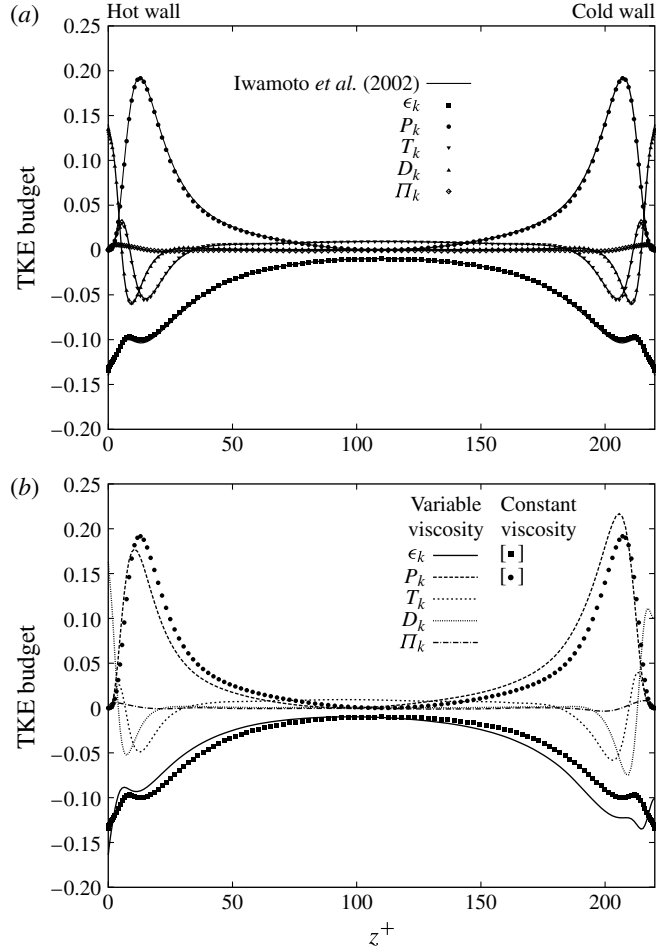
FIGURE 12. Budget of TKE: (*a*) simulation $S1.1$; (*b*) simulation $S1.3$. In (*a*) lines represent reference data from validation database of Iwamoto *et al.* (2002); symbols represent present calculations.

of viscosity near the cold wall. As for the other budget terms, only viscous diffusion shows non-negligible changes: D_k increases at the hot wall whereas a decrease of D_k associated with an inflection point is observed at the cold wall.

The present findings put the statistical description of the turbulent flow field and the phenomenological causal dynamics of the coherent structures given in the previous sections on a firmer ground. They explain, for instance, the behaviour of the wall-normal component of the skewness factor $\langle S(u'_z) \rangle$, which increases (respectively decreases) near the hot wall (respectively cold wall), as shown in figure 6(*b*), and thus may be used to analyse further the streaky structures near the walls. As mentioned, the ratio between production and dissipation defines the so-called 'local' shear rate $\tilde{S} = P_k/\epsilon_k$, a non-dimensional parameter which bears useful information about the conditions under which streaks strengthen or weaken (Lam & Banerjee 1992). The critical condition to ensure streak formation is $\tilde{S} > 1$: as $\tilde{S}$ gets larger, streaks become more evident and persistent. The wall-normal evolution of $\tilde{S}$ in our simulations is
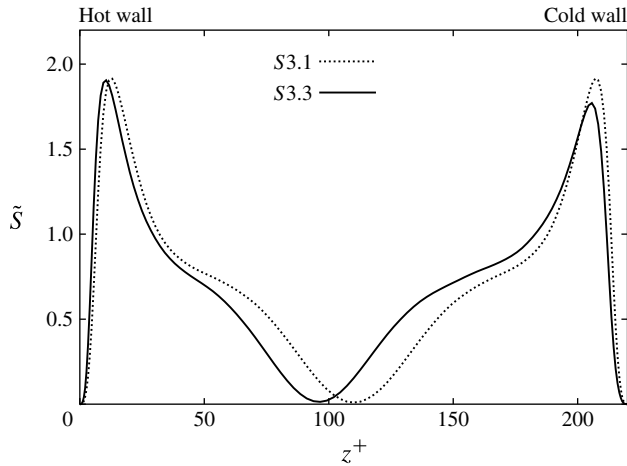
FIGURE 13. Wall-normal profiles of non-dimensional shear rate $\tilde{S}$.

given in figure 13. In the constant-viscosity simulation ($S1.1$, dashed line), $\tilde{S}$ is equal to zero at the wall, reaches a peak value of ~ 1.92 in the near-wall region and then vanishes in the centre of the channel. In the variable-viscosity simulation ($S1.3$, solid line), the qualitative behaviour is the same except that $\tilde{S}$ increases (respectively decreases) in the fluid slab comprised between the hot wall (respectively cold wall) and the closest location at which the peak value $\tilde{S} \simeq 1.85$ (respectively $\tilde{S} \simeq 1.77$) occurs. Note that the thickness of the region where $\tilde{S} > 1$ near the cold wall is larger than near the hot wall. In the centre of the channel, where $\tilde{S} < 1$, a change of viscosity makes $\tilde{S}$ decrease toward the hot side and increase toward the cold side. These modifications of $\tilde{S}$ are functional to explain the behaviour of the streaky structures shown in figure 8, where streaks become less evident in the regions where production reduces relative to dissipation. Another way to consider the significance of $\tilde{S}$ is to notice that it provides a measure of the degree of anisotropy of the turbulent motions combined to a measure of the rate of deformation of the fluid imposed by the mean shear rate. The critical condition for $\tilde{S}$ thus means that streaks can become more persistent if the mean deformation is sufficiently rapid compared with turbulent fluctuations and/or significant shear component of the turbulent stresses exist (Lam & Banerjee 1992). This is roughly what we observe at the hot wall, and exactly the opposite of what we observe at the cold wall.

4. Conclusions and future developments

Convective heat transfer in turbulent shear flows is characterized by complex macroscopic phenomena that are rich in physics yet difficult to model and/or to reproduce. Complexity becomes particularly clear in situations where the thermophysical properties of the fluid depend strongly on temperature. This is the case of water-based convective heat transfer equipments, in which the occurrence of large temperature gradients produces significant variations of density, dynamic viscosity and thermal conductivity. In this paper, we focus on the effects produced by temperature-dependent fluid viscosity, isolated from gravity, on the flow field in turbulent forced convection. To study these effects, which are relevant for aerospace applications,

we performed numerical experiments based on an extensive campaign of direct simulations of convective heat transfer in turbulent channel flow with temperature-dependent viscosity. Simulations were run at Reynolds numbers $Re_\tau = 110$, 150, 180 and 300 and Prandtl number $Pr = 3$. Comparison against companion constant-viscosity simulations is made for the case of constant-temperature boundary conditions. The temperatures at the hot wall, T_H^*, and at the cold wall, T_C^*, were varied to generate temperature differences between walls ($T_H^* - T_C^* = 40$ and 60 K) while maintaining a constant average temperature, $(T_H^* + T_C^*)/2$. Having neglected gravity, we have been able to emphasize the non-trivial behaviour due to variable viscosity and the way it is modulated by a change in Re_τ. The effects we observe in zero-gravity conditions fade out as Re_τ increases: for low Reynolds numbers, however, the same effects are found in Earth gravity conditions, e.g. in stable stratification problems (Zonta 2010; Zonta *et al.* 2012).

When compared against with constant-viscosity simulations, the statistical moments for the fluid velocity obtained with temperature-dependent viscosity exhibit significant differences throughout the entire channel, particularly in the near-wall regions. Counterintuitively, we find that turbulence is promoted in the cold side of the channel, where viscosity is higher; turbulence is damped in the hot side of the channel, where viscosity is lower. The increase of viscosity near the cold wall, in particular, enhances TKE, while reducing the mean velocity gradient. An opposite behaviour is observed at the hot wall, where viscosity attains lower-than-mean values and turbulence is damped due to higher viscous dissipation. In addition fluctuations at the hot wall become more intermittent, a situation that is encountered also outside the buffer region within the cold side of the channel. We have justified these observations with scaling arguments based on local viscosity effects on the inertial and viscous forces of the flow. We have also provided qualitative explanation of the observed statistical behaviour based on examination of the instantaneous flow structures in the near-wall region. We find that streak characteristics, spacing and length, change between the hot wall and the cold wall. Also, bursting frequencies are altered: compared with the constant-viscosity case, the time between two subsequent sweep/ejection events increases at the hot wall and decreases at the cold wall. The cross-over point from sweeps dominance to ejections dominance in the hot side (respectively cold side) of the channel shifts to reduce (respectively expand) the sweep-dominated region near the wall, all of this leading to drag reduction (respectively increase) and to different density in the spatial distribution of the quasi-streamwise vortices, which appear larger and more frequent near the cold wall than near the hot wall. This behaviour is common to all cases with temperature-dependent viscosity covered by the present study.

We have also examined the TKE budgets, to investigate the mechanisms of turbulence production, dissipation and transport in the presence of anisotropic fluid viscosity. Our findings indicate that the macroscopic flow behaviour and the microscopic features of the turbulent field can be explained by modifications of the turbulence production and dissipation mechanisms near the two walls. Moving from the central region of the channel toward the hot wall, both production and dissipation decrease. Very close to the hot wall, the decrease of viscosity no longer affects production but is high enough to increase dissipation with respect to the case of constant viscosity. In the cold side of the channel, production and dissipation increase reaching a maximum value a few viscous units from the wall. Moving further toward the wall, the increase of viscosity reduces dissipation significantly compared with the constant-viscosity case while leaving production practically unchanged. As a result, the ratio between production and dissipation increases near the hot wall and decreases near

the cold wall, where more favourable conditions for streak formation and persistence are found.

Present findings apply to forced-convection turbulent heat transfer in the absence of gravity (e.g. stratification) effects. Further step of this study will be the inclusion of variable thermal conductivity and coefficient of thermal expansion, which at present times have been investigated mostly for Rayleigh–Bénard convection problems (see, for instance, Shishkina & Thess 2009; Stevens, Verzicco & Lohse 2010, and references therein). Many questions concerning the effects produced by temperature-dependent fluid properties on mixed convection in stratified shear flow remain open and demand further analysis. We also believe that our study may provide information useful for developing reliable two-phase mixture models for the prediction of turbulent forced convection of nanofluids, in which the dependence of viscosity on both temperature and nanoparticle volume concentration is explicitly taken into account (Behzadmehr, Saffar-Avval & Galanis 2007). Finally, we remark that current results are obtained at a constant pressure gradient. It is perhaps non-straightforward to derive conclusions on experiments run at a constant flow rate, which deserve an independent investigation.

Appendix. Description of the numerical methodology

The algorithm employed in this study is based on the following solution procedure.

A.1. *Velocity field calculation*

We solve for the following time-differenced Navier–Stokes equations obtained from the Fourier transform of (2.3):

$$\frac{\hat{u}_i^{n+1} - \hat{u}_i^n}{\Delta t} = \frac{3}{2}\hat{S}_i^n - \frac{1}{2}\hat{S}_i^{n-1} + \frac{1}{Re_\tau}\frac{\partial^2}{\partial x_j \partial x_j}\left(\frac{\hat{u}_i^{n+1} + \hat{u}_i^n}{2}\right) - \frac{\partial}{\partial x_i}\left(\frac{\hat{p}^{n+1} + \hat{p}^n}{2}\right), \quad \text{(A 1)}$$

where $S_i = -u_j(\partial u_i/\partial x_j) + \delta_{i,1} + (1/Re_\tau)(\partial/\partial x_j)(\mu_v \partial u_i/\partial x_j)$ and superscript n represents the time step. Note that an implicit Crank–Nicolson scheme is used for the uniform part of the viscous terms, while an explicit Adams–Bashforth scheme is used for both the non-uniform part of the viscous terms and the nonlinear terms S_i. Taking the curl of (A 1) and dropping superscript $n + 1$ for the unknown variables, the following second-order differential equation for the wall-normal component of vorticity, $\hat{\omega}_z$, is obtained

$$\left(\frac{\partial^2}{\partial z^2} - \frac{1 + \gamma^2}{\gamma}\right)\hat{\omega}_z = -\frac{1}{\gamma}\left(ik_x \hat{H}_y - ik_y \hat{H}_x\right), \quad \text{(A 2)}$$

where $\gamma = \Delta t/2Re_\tau$, k_x and k_y are the Fourier wavenumbers, and terms $\hat{H}_i$ group all working variables evaluated at time steps n and $n - 1$. Taking twice the curl of (A 1), the wall-normal velocity component can be obtained from the following fourth-order equation:

$$\left(\frac{\partial^2}{\partial z^2} - \frac{1 + \gamma^2}{\gamma}\right)\left(\frac{\partial^2}{\partial z^2} - k^2\right)\hat{u}_z = \frac{\hat{H}}{\gamma}, \quad \text{(A 3)}$$

where $\hat{H} = k^2\hat{H}_z + \partial(ik_x\hat{H}_x + ik_y\hat{H}_y)/\partial z$ and $k^2 = k_x^2 + k_y^2$. Equations (A 2) and (A 3) are of Helmholtz type and are solved using a Chebyshev–Tau method. Once $\hat{\omega}_z$ and $\hat{u}_z$ are available, $\hat{u}_x$ and $\hat{u}_y$ can be obtained from the definition of wall-normal vorticity:

$$-ik_y\hat{u}_x + ik_x\hat{u}_y = \hat{\omega}_z, \qquad (A\,4)$$

and from the discretized form of the continuity equation:

$$ik_x\hat{u}_x + ik_y\hat{u}_y = -\frac{\partial\hat{u}_z}{\partial z}. \qquad (A\,5)$$

Such a procedure ensures mass conservation at each time step. Dirichlet boundary conditions are applied in the solution procedure to satisfy the no-slip restriction at the walls. The numerical implementation is based on that of Lam & Banerjee (1992).

A.2. *Temperature field calculation*

The time-differenced energy equation (2.4) reads as

$$\frac{\hat{T}_i^{n+1} - \hat{T}_i^n}{\Delta T} = \frac{3}{2}\hat{S}_T^n - \frac{1}{2}\hat{S}_T^{n-1} + \frac{1}{PrRe_\tau}\frac{\partial^2}{\partial x_j\partial x_j}\left(\frac{\hat{T}_i^{n+1} + \hat{T}_i^n}{2}\right), \qquad (A\,6)$$

where $S_T = -u_j(\partial T/\partial x_j)$. Upon transforming (A 6) in the wavenumber space, temperature $\hat{T}$ can be obtained from the following differential equation:

$$\left(\frac{\partial^2}{\partial z^2} - \frac{1 + \gamma_T^2}{\gamma_T}\right)\hat{T} = -\frac{\hat{H}_T}{\gamma_T}, \qquad (A\,7)$$

where $\gamma_T = \Delta t/(2Pr\cdot Re_\tau)$ and $\hat{H}_T = [\gamma_T\partial^2/\partial z^2 + (1 - \gamma_T k^2)]\hat{T}^n + \Delta T(3\hat{S}_T^n/2 - \hat{S}_T^{n-1}/2)$. Equation (A 7) is solved with the Chebyshev–Tau method to update the temperature field. Dirichlet boundary conditions are applied to impose wall temperature, mimicking the situation in which heat is supplied from a source (the hot wall) and released to a sink (the cold wall).

A.3. *Viscosity field update*

Once $\hat{T}^{n+1}$ is available, viscosity is updated to its new value through (2.5). Finally, all working variables are initialized for calculation of the next time step and the algorithm loops back to § A.1.

REFERENCES

ADRIAN, R. J. 2007 Hairpin vortex organization in wall turbulence. *Phys. Fluids* **19**, 041301.

BAE, J. H., YOO, Y. J. & CHOI, H. 2005 Direct numerical simulation of supercritical flows with heat transfer. *Phys. Fluids* **17**, 105104.

BEHZADMEHR, A., SAFFAR-AVVAL, M. & GALANIS, N. 2007 Prediction of turbulent forced convection of a nanofluid in a tube with uniform heat flux using a two phase approach. *Intl J. Heat Fluid Flow* **28**, 211–219.

BERNARD, P. S., THOMAS, J. M. & HANDLER, R. A. 1993 Vortex dynamics and the production of Reynolds stress. *J. Fluid Mech.* **253**, 385–419.

BUYUKALAKA, O. & JACKSON, J. D. 1998 The correction to take account of variable property effects on turbulent forced convection to water in a pipe. *Intl J. Heat Mass Transfer* **41**, 665–669.

CAMPOLO, M., ANDREOLI, M. & SOLDATI, A. 2009 Computing flow, combustion, heat transfer and thrust in a micro-rocket via hierarchical decomposition. *Microfluid Nanofluid* **7**, 57–73.

IWAMOTO, K., SUZUKI, Y. & KASAGI, N. 2002 Reynolds number effect on wall turbulence: toward effective feedback control. *Intl J. Heat Fluid Flow* **23**, 678–689.

KANG, S., IACCARINO, G. & HAM, F. 2009 DNS of buoyancy-dominated turbulent flows on a bluff body using the immersed boundary method. *J. Comput. Phys.* **228**, 3189–3208.

KIM, J., MOIN, P. & MOSER, R. 1987 Turbulence statistics in fully-developed channel flow at low Reynolds number. *J. Fluid Mech.* **177**, 133–166.

LAM, K. & BANERJEE, S. 1992 On the condition of streak formation in bounded flows. *Phys. Fluids* A **4**, 306–320.

LEE, J., GHARAGOZLOO, P. E., KOLADE, B., EATON, J. K. & GOODSON, K. E. 2010 Nanofluid convection in microtubes. *Trans. ASME J. Heat Transfer* **132**, 092401.

LI, X., HASHIMOTO, K., TOMINAGA, Y., TANAHASHI, M. & MIYAUCHI, T. 2008 Numerical study of heat transfer mechanism in turbulent supercritical CO_2 channel flow. *J. Therm. Sci. Tech. - JPN* **3**, 112–123.

LOMBARDI, P., DE ANGELIS, V. & BANERJEE, S. 1996 Direct numerical simulation of near-interface turbulence in coupled gas–liquid flow. *Phys. Fluids* **8**, 1643–1665.

LUCHIK, T. S. & TIEDERMAN, W. G. 1987 Time scale and structure of ejections and bursts in turbulent channel flows. *J. Fluid Mech.* **174**, 529–552.

MAIGA, S. E. B., PALM, S. J., NGUYEN, C. T., ROY, G. & GALANIS, N. 2005 Heat transfer enhancement by using nanofluids in forced convection flows. *Intl J. Heat Fluid Flow* **468**, 283–315.

MARCHIOLI, C., SOLDATI, A., KUERTEN, J. G. M., ARCEN, B., TANIERE, A., GOLDENSOPH, G., SQUIRES, K. D., CARGNELUTTI, M. F. & PORTELA, L. M. 2008 Statistics of particle dispersion in direct numerical simulations of wall-bounded turbulence: results of an international collaborative benchmark test. *Intl J. Multiphase Flow* **34**, 879–893.

MARCHIOLI, C. & SOLDATI, A. 2002 Mechanisms for particle transfer and segregation in turbulent boundary layer. *J. Fluid Mech.* **468**, 283–315.

MONIN, A. S. & YAGLOM, A. M. 1975 *Statistical Fluid Mechanics: Mechanism of Turbulence, book 2*. MIT Press.

PAN, Y. & BANERJEE, S. 1995 A numerical study of free-surface turbulence in channel flow. *Phys. Fluids* **7**, 1649–1664.

PERRY, A. & CHONG, M. S. 1987 A description of eddying motions and flow patterns using critical point concepts. *Annu. Rev. Fluid Mech.* **9**, 125–148.

PINARBASI, A., OZALP, C. & DUMAN, S. 2005 Influence of variable thermal conductivity and viscosity for nonisothermal fluid flow. *Phys. Fluids* **17**, 038109.

POPIEL, C. O. & WOJTKOWIAK, J. 1998 Simple formulas for thermophysical properties of liquid water for heat transfer calculations (from 0 °C to 150 °C). *Heat Transfer Engng* **19** (3), 87–101.

SAMEEN, A. & GOVINDARAJAN, R. 2007 The effect of wall heating on instability of channel flow. *J. Fluid Mech.* **577**, 417–442.

SEWALL, E. A. & TAFTI, D. K. 2008 A time-accurate variable property algorithm for calculating flows with large temperature variations. *Comput. Fluids* **37**, 51–63.

SHIN, S. Y., CHO, Y. I., GRINGRICH, W. K. & SHYY, W. 1993 Numerical study of laminar heat transfer with temperature dependent fluid viscosity in a 2:1 rectangular duct. *Intl J. Heat Mass Transfer* **36**, 4365–4373.

SHISHKINA, O. & THESS, A. 2009 Mean temperature profiles in turbulent Rayleigh–Bénard convection of water. *J. Fluid Mech.* **633**, 449–460.

SIEDER, E. N. & TATE, G. E. 1936 Heat transfer and pressure drop of liquids in tubes. *Ind. Engng Chem.* **28**, 1429–1435.

SOLDATI, A. 2005 Particles turbulence interactions in boundary layers. *Z. Angew. Math. Mech.* **85**, 683–699.

SOLDATI, A. & BANERJEE, S. 1998 Turbulence modification by large-scale organized electrohydrodynamic flows. *Phys. Fluids* **10**, 1743–1756.

STEVENS, R. J. A. M., VERZICCO, R. & LOHSE, D. 2010 Radial boundary layer structure and Nusselt number in Rayleigh–Bénard convection. *J. Fluid Mech.* **643**, 495–507.

VERZICCO, R. & SREENIVASAN, K. R. 2008 A comparison of turbulent thermal convection between conditions of constant temperature and constant heat flux. *J. Fluid Mech.* **595**, 203–219.

WEAST, R. C. 1988 *CRC Handbook of Chemistry and Physics*. CRC Press.

WILLMARTH, W. W. & LU, S. S. 1972 Structure of the Reynolds stress near the wall. *J. Fluid Mech.* **55**, 65–92.

YU, W., FRANCE, D. M., TIMOFEEVA, E. V., SINGH, D. & ROUTBORT, J. L. 2010 Thermophysical property-related comparison criteria for nanofluid heat transfer enhancement in turbulent flow. *Appl. Phys. Lett.* **96**, 213109.

ZONTA, F. 2010 Turbulence and thermal stratification in inhomogeneous shear flows. PhD thesis, University of Udine, Udine (Italy).

ZONTA, F., MARCHIOLI, C. & SOLDATI, A. 2008 Direct numerical simulation of turbulent heat transfer modulation in micro-dispersed channel flow. *Acta Mech.* **195**, 305–326.

ZONTA, F., ONORATO, M. & SOLDATI, A. 2012 Turbulence and internal waves in stably-stratified channel flows with temperature-dependent fluid properties. *J. Fluid Mech.* **697**, 175–203.